Co valence transformation in isopolar $LaCoO_3/LaTiO_3$ perovskite heterostructures via interfacial engineering

Georgios Araizi-Kanoutas,[1,*,†] Jaap Geessinck,[2,*] Nicolas Gauquelin,[3] Steef Smit,[1] Xanthe H. Verbeek,[1] Shrawan K. Mishra,[4] Peter Bencok,[5] Christoph Schlueter,[6] Tien-Lin Lee,[5] Dileep Krishnan,[3] Jarmo Fatermans,[3,7] Jo Verbeeck,[3] Guus Rijnders,[2] Gertjan Koster,[2] and Mark S. Golden[1,‡]

[1]*Van der Waals–Zeeman Institute for Experimental Physics, Institute of Physics, University of Amsterdam, Science Park 904, 1098 XH Amsterdam, Netherlands*

[2]*MESA+ Institute for Nanotechnology, University of Twente, Faculty of Science and Technology, P.O. Box 217, 7500 AE Enschede, Netherlands*

[3]*Electron Microscopy for Materials Science, University of Antwerp, Campus Groenenborger, Groenenborgerlaan 171, 2020 Antwerpen, Belgium*

[4]*School of Materials Science and Technology, Indian Institute of Technology (BHU), Varanasi 221 005, India*

[5]*Diamond Light Source, Limited, Diamond House, Harwell Science and Innovation Campus, Didcot OX11 0DE, United Kingdom*

[6]*PETRA III, DESY Photon Science, Notkestrasse 85, 22607 Hamburg, Germany*

[7]*Imec-Vision Lab, University of Antwerp, Campus Drie Eiken, Universiteitsplein 1, 2610 Wilrijk, Belgium*

(Received 2 September 2019; revised manuscript received 28 November 2019; accepted 14 January 2020; published 10 February 2020)

We report charge transfer up to a single electron per interfacial unit cell across nonpolar heterointerfaces from the Mott insulator $LaTiO_3$ to the charge transfer insulator $LaCoO_3$. In high-quality bi- and trilayer systems grown using pulsed laser deposition, soft x-ray absorption, dichroism, and scanning transmission electron microscopy-electron energy loss spectroscopy are used to probe the cobalt-3*d* electron count and provide an element-specific investigation of the magnetic properties. The experiments show the cobalt valence conversion is active within 3 unit cells of the heterointerface, and able to generate full conversion to $3d^7$ divalent Co, which displays a paramagnetic ground state. The number of $LaTiO_3/LaCoO_3$ interfaces, the thickness of an additional, electronically insulating "break" layer between the $LaTiO_3$ and $LaCoO_3$, and the $LaCoO_3$ film thickness itself in trilayers provide a trio of control knobs for average charge of the cobalt ions in $LaCoO_3$, illustrating the efficacy of *O*-2*p* band alignment as a guiding principle for property design in complex oxide heterointerfaces.

DOI: 10.1103/PhysRevMaterials.4.026001

I. INTRODUCTION

Complex oxides of the transition metals are of great importance and interest from both a technological and a fundamental science point of view. Technologically, $LiCoO_2$ has underpinned the development of the now eponymous Li ion battery [1], ferrites are indispensable in transformer cores and inductors, and oxide piezoelectric materials, such as PZT and their Pb-free analogs, are enablers of ultrasound imaging [2,3]. With regard to fundamental science, complex oxides show an interplay between strong electron correlations, band behavior, and a rich repertoire of ordering phenomena in the spin and orbital sectors, making them an enduring focus of theoretical and experimental investigation [4,5].

The maturity of epitaxy-based thin-film growth techniques provides opportunities to improve experimental control over the properties of these systems, leading to emergent interfacial properties such as conductivity [6], magnetism [7], and superconductivity [8,9]. A central concept in the field is the role played by nature's response to an incipient polar catastrophe at interfaces, which can be seen as an ultimate driver of interfacial charge transfer [10], providing an elegant and powerful new mechanistic paradigm for doping at a distance in an interfacial system. In practice, the response of real materials to the presence of a potentially polar interface can also be rooted in the relatively facile creation of oxygen vacancies in perovskite transition metal oxides [11], meaning in some systems the in-built potential of a polar overlayer is observed [12], and in other cases, such as the $LaAlO_3$ (LAO)/$SrTiO_3$ (STO) system, it is not [13]. In addition, strain and the $GdFeO_3$ (or octahedral tilting) distortion of the cubic ABO_3 perovskite can also be either transmitted or blocked between a bulk substrate and an overlayer [14]. All of these and other properties constitute a number of tools that can be used to design interesting and potentially useful functionalities in complex oxides [15]. As the dominant, silicon-based electronic materials universe makes clear, the interface can indeed be the device [16], fostering added interest in (ultra)thin oxide films and their interfacial properties.

One method to tune and control *d*-state occupation is via charge transfer, and recently, a broadly applicable principle

*These authors contributed equally to this work.
†g.araizikanoutas@uva.nl
‡m.s.golden@uva.nl

was introduced, enabling the design of oxide heterointerfaces in which charge transfer is predicted [17]. The idea here is that both the octahedral backbone and the *A*-site sublattice in an ABO_3 perovskite can be considered continuous across an $ABO_3/AB'O_3$ heterointerface. As a consequence, the O-2*p*-related bands of the two materials should align in energy. Depending on the relative energy alignment and separation of the metal (*B* or *B*′) 3*d* and O-2*p* states in each compound, this can lead to charge transfer becoming favorable in the heterointerface, and also in the case of *isopolar* heterointerfaces. The observation [18] of divalent Fe at isopolar interfaces between $LaTiO_3$ (LTO) (ground state $3d^1$) and $LaFeO_3$ (ground state $3d^5$) was an important inspiration for the development of the O-2*p* band alignment picture [17]. The band alignment argument presents a clear driving force for nature to avoid a d^6 $LaCoO_3$ (LCO)/d^1 LTO interface. Recently, the propensity of LTO to overoxidize was highlighted [19], and this can be seen as an alternative route for Ti to take on a $3d^0$ configuration in the LCO/LTO interface.

In this paper, we report the successful generation of interfacial, valence-transformed, divalent cobalt ions in LCO. This charge state is realized without any cationic chemical doping or visible change in the structure, and is operative at the nanoscale, concentrated within 3 unit cells of the LCO/LTO interface. By tuning the LCO thickness and number of interfaces, the average Co valence can be altered between di- and trivalent. This electronic transformation of the Co $3d^6$ to a $3d^7$ state goes hand in hand with significantly increased paramagnetic polarization in external magnetic fields.

We present detailed spectroscopic and scanning transmission electron microscopy (STEM) data from a variety of LCO/LTO interfacial systems. These data not only characterize the cobalt valence transformation but also enable a discussion of the two main mechanistic routes for Co-$3d^6$ generation, namely O-2*p* band alignment driven charge transfer from LTO, and/or (overoxidation) underoxidation of the (LTO) LCO layers.

As we will present in detail below, key facets of the experimental data support the picture where electronic charge transfer is important, while other data point to the presence of oxygen nonstoichiometry. Therefore, while accepting the reality of oxygen off-stoichiometry effects in real-life perovskite transition metal oxides, these experimental findings support the design guidelines involving O-2*p* band alignment as a driving force for the generation of interfaces with tailored charge/orbital states [17]. Nanoscale, controlled electron transfer processes in oxides—in particular, in cobaltates—could also be very interesting in the context of sustainable energy technologies involving the oxygen evolution reaction, in which activity has been linked to an e_g electron occupancy of unity [20].

II. SAMPLE DESIGN AND FABRICATION

LCO can be considered the parent compound of many interesting complex cobalt oxides. In its ground state, bulk LCO is a d^6 charge transfer insulator with a nominally low-spin, nonmagnetic configuration ($t_{2g}^6 e_g^0$). Early temperature-dependent studies [21] suggested a gradual transition from low-spin (LS) to intermediate-spin (IS) states, but more recent studies were clear that the LS ground state coexists with a triply degenerate high-spin (HS) excited state, to yield an inhomogeneous mixed-spin state [22]. In the experiments reported here, ultrathin films of LTO and LCO were grown using pulsed laser deposition (PLD) on conducting 0.5 wt. % Nb-doped, (100)-oriented STO substrates. The substrates were ultrasonically cleaned in acetone and subsequently ethanol, followed by a chemical etching procedure and finally annealing to achieve a well-defined, single TiO_2-terminated surface [23]. Intensity variations in reflection high-energy electron diffraction (RHEED) were used to monitor the growth and assure unit cell (uc) level control over the film thickness. Subsequently, a 30 uc thick layer of LAO was grown. This served to (a) enable an accurate calibration of the PLD setup as LAO grows very well in a layer-by-layer manner; (b) prevent formation of a polar-interface-driven charge transfer involving the LCO or LTO (both of which are polar) by separating them far from the nonpolar STO; (c) mask the Ti states of the STO substrate in the soft x-ray absorption experiments; and (d) discourage transport of oxygen from the STO substrate into the LTO film [19]. After growth of the LTO, LCO, or combinations thereof, a 5 uc $LaNiO_3$ (LNO) layer was added as a cap. The addition of this layer could be seen as a complication, yet it was a precautionary measure taken to hinder oxygen off-stoichiometry due to atmospheric exposure and to structurally "close" the perovskite structure of the top layer of the single-, bi-, or trilayer. An LAO cap was tried, but led to deleterious charging effects, particularly for the low-temperature experiments probing the magnetic properties, and thus LNO was adopted throughout.

The growth of LCO and LTO film combinations poses a dilemma: in order to grow LTO, a low oxygen background pressure (typically well below 10^{-4} mbar) is desired, in order to avoid formation of unwanted phases like $La_2Ti_2O_7$ [24] and overoxidation of the LTO, which results in tetravalent Ti with $3d^0$ electronic configuration [19]. On the other hand, good LCO growth prefers a higher oxygen background pressure (typically ∼0.1 mbar), so as to avoid oxygen vacancies [25]. Thus, while interfacing perfect, stoichiometric LTO and LCO in the computer [17] is relatively straightforward, in the laboratory, true high-pressure LCO growth would aggressively overoxidize the underlying LTO, resulting in an uncontrolled LTO quality, and low-pressure growth aimed at stoichiometric LTO will not allow the growth of stoichiometric LCO with trivalent Co. Consequently, a third way was chosen here, namely, to grow both materials at an intermediate pressure of 2×10^{-3} mbar. The LTO thickness was kept below 5 uc, and the substrate-induced strain was used to help stabilize the 113 phase of LTO [25]. We note that all LCO reference samples grown without LTO were still grown at this intermediate pressure to facilitate comparison. Other PLD parameters were optimized to obtain a flat and smooth surface after deposition and to form sharp interfaces. Ideally, additional trilayers in which the LTO thickness was varied with constant LCO thickness could be instructive. However, in practice, the formation of unwanted, non-113 LTO phases in these systems and the inability to fully reach the LCO layer using total electron yield x-ray absorption spectroscopy (TEY XAS) for thicker LTO layers form prohibitively severe complications to their study.

TABLE I. PLD growth parameters for the LAO, LTO, LCO, and LNO layers. $P(O_2)$ denotes the oxygen background pressure during growth.

Material	Fluence (J/cm^2)	Substrate temperature (°C)	Laser repetition rate (Hz)	$P(O_2)$ (mbar)	Laser spot size (mm^2)
$LaAlO_3$	1.3	750	1	2×10^{-3}	2.3
$LaTiO_3$	1.9	750	1	2×10^{-3}	2.3
$LaCoO_3$	1.9	850	2	2×10^{-3}	2.3
$LaNiO_3$	1.9	750	1	2×10^{-3}	2.3

An overview of all the growth parameters can be found in Table I. Below we will experimentally justify the appropriateness of the chosen synthesis conditions.

A wide range of samples were grown, designed to test various aspects of the expected physical behavior. As mentioned above, all possess a 30 uc LAO buffer layer and a 5 uc LNO capping layer and can be divided into four differing sample types as depicted in Fig. 1.

The four sample types are as follows:

(a) LCO: containing no interface (0IF).

(b) LTO/LCO: containing a single heterointerface (1IF), a $4/x$ sample.

(c) LTO/LCO/LTO: containing a double heterointerface (2IF), a $4/x/4$ sample.

(d) LTO/LAO/LCO: a single-interface system including a "breaker" layer of LAO.

To exclude strain-related effects dominating the physics observed, a 2IF sample was also generated on an LAO substrate.

Since the bulk (pseudocubic) lattice constant of LCO is 3.78 Å at 4 K and 3.84 Å at 1248 K [26] the LCO would have a tensile strain of about 3% when fully strained on the STO substrates. For the samples grown on bulk (100) LAO substrates, LCO would have a compressive strain of about 1%.

III. SOFT X-RAY ABSORPTION, X-RAY MAGNETIC CIRCULAR DICHROISM, AND HARD X-RAY PHOTOEMISSION

XAS was carried out at the Co-$L_{2,3}$ (and Ti-$L_{2,3}$) edges using soft x rays from the I10 beamline at Diamond Light Source, Didcot, in the BLADE end station. Both TEY and fluorescence yield (FY) detection modes were employed simultaneously. The TEY signal exhibits an exponential falloff as a function of the depth into the sample. The inelastic mean-free path, describing the characteristic length scale on which the signal is attenuated by a factor of $1/e$ compared to the incident value, is about 4 nm at the Co-L_3 edge [27] in TEY, meaning 95% of the signal is from within 12 nm from the surface. The effective FY probing depth is comparable to the x-ray penetration depth, but FY data do present some complications for the use of x-ray magnetic circular dichroism (XMCD) sum rules [28], so the XMCD data analysis presented here concerns the TEY data. The experimental station combines a cryostat operated at a lowest temperature of 10 K with a superconducting magnet applying fields between $-14 \leqslant H \leqslant +14$ teslas. The magnetic field is oriented along the incoming x-ray beam path, facilitating element-specific magnetometry based on XMCD experiments. The base pressure of the measurement chamber is in the 10^{-10} mbar range.

The $L_{2,3}$-edge XAS spectrum of a transition metal compound involves electronic transitions from the $2p_{1/2}$ and $2p_{3/2}$ core levels to unoccupied $3d$ states, and provides an ultrasensitive fingerprint of the d-electron count, or valence of the system under investigation [29].

For ensuring maximally accurate XAS data, experiments were conducted at 10 K by recording repeated blocks of spectra with alternating x-ray polarization (e.g., σ^+-σ^--σ^+ followed by σ^--σ^+-σ^-). For the valence fingerprinting, the average of the spectra for the two circular polarizations is taken. For the majority of the data reported here, the x rays were incident at a grazing angle of 20° with respect to the surface of the film. Control experiments were carried out at higher temperatures, larger incidence angles, and investigating different locations on the 5×5 mm^2 films. In all cases,

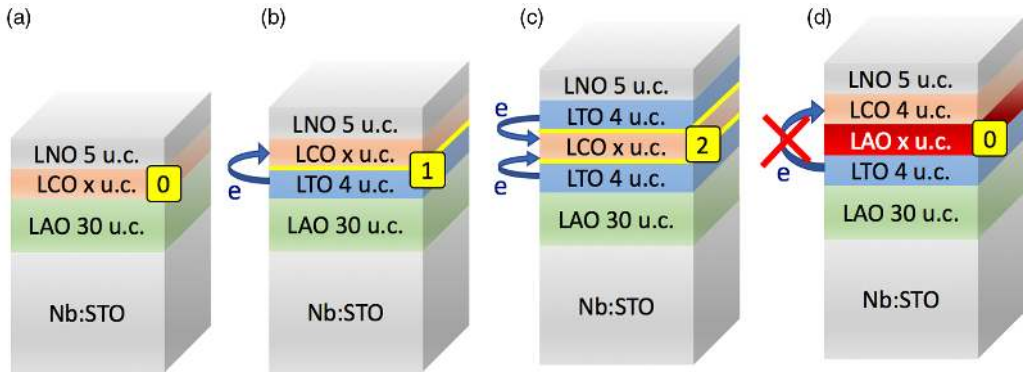

FIG. 1. Family of samples according to the number of "active" $LaTiO_3/LaCoO_3$ interfaces (IFs) (yellow highlight): (a) no LTO/LCO IF (0IF); (b) (1IF) LTO/LCO; (c) (2IF) LTO/LCO; (d) no direct LTO/LCO IF (0IF) due to LAO "break" layer. All samples were grown on Nb:STO substrates with an LAO buffer layer of 30 uc and a 5 uc LNO cap.

the measured XAS spectra were normalized to the edge jump, accounting for the number of holes in the $3d$ shell, while a linear background that was determined well before the pre-edge region was subtracted.

Hard x-ray photoemission spectroscopy (HAXPES) measurements were conducted at the I09 beamline at Diamond Light Source using a photon energy of 2.2 keV. The HAXPES spectra were recorded using an EW4000 photoelectron analyzer (VG Scienta), equipped with a wide-angle acceptance lens, with the x rays incident at a grazing angle of 55°, so as to enable depth profiling analysis of the photoelectrons where appropriate. XAS spectra were also recorded at the I09 beamline at the Co-$L_{2,3}$ edges from the same spot (30 μm × 50 μm) as was measured using HAXPES, so as to connect to the XAS data recorded at the I10 beamline. A portable ultra high vacuum (UHV) "suitcase" chamber was used to transfer some of the samples from the PLD system in Twente to Diamond in a pressure in the 10^{-10} mbar range, to investigate whether oxidation occurs during transport.

The *in situ* x-ray photoemission spectroscopy (XPS) data shown in the Supplemental Material [30] (Fig. S4) were recorded in the Twente multichamber PLD system using monochromatized Al-$K\alpha$ radiation and an Omicron 7-channeltron electron energy analyzer.

IV. SCANNING TRANSMISSION ELECTRON MICROSCOPY

STEM using high-angle annular dark field (HAADF) imaging was performed using a FEI Titan 80-300 microscope operated at 120 kV. The samples were prepared in a vacuum transfer box and studied while held in a Gatan vacuum transfer sample holder to avoid any influence of air on the film [31–33]. Electron energy loss spectroscopy (EELS) measurements were performed using a monochromatic beam with a 120 meV energy resolution. The Ti-L, Co-L, O-K, and La-M_5 edges were acquired simultaneously (the La being used for energy calibration). The acquisition parameters were 0.25 s/pixel, 0.4 Å/pixel, and 0.05 eV/pixel in the dual EELS mode. Collection angles for HAADF imaging and EELS were 70–160 mrad and 47 mrad, respectively.

V. RESULTS AND DISCUSSION

A. XAS data

As panel (b) of Fig. 2 shows, Co-$L_{2,3}$ XAS spectra from high-quality single crystals taken from Ref. [34] are very characteristic for whether the cobalt ions are trivalent (nominally d^6, in this case $EuCoO_3$ or Sr_2CoO_3Cl) or divalent (formally d^7, here CoO). There are some subtle differences between the LS and HS variants in the trivalent case, but there are two very prominent low-energy features in the divalent case, highlighted with yellow arrows that make a valence change from tri- to divalent experimentally very easy to spot.

Panel (a) of Fig. 2 shows the core result of this research. The data from the thin (4 uc) film of LCO (blue) closely resembles a combination of the spectra of the two trivalent model compounds [35]. Upon sandwiching a sample with 2 uc of LCO between LTO layers to generate *two* LTO/LCO interfaces (2IF) (red), strong XAS intensity can be seen at the

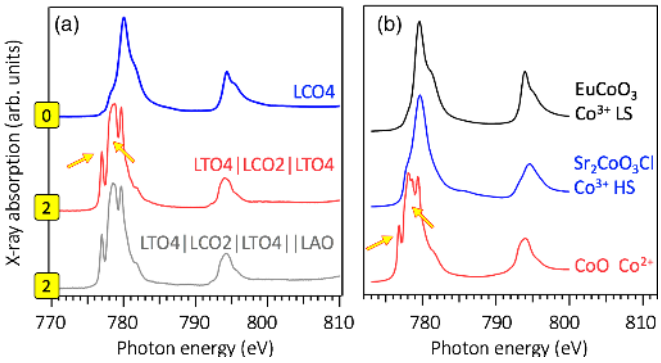

FIG. 2. Valency fingerprinting via Co-$L_{2,3}$ XAS shows complete transformation to divalent Co. (a) From top to bottom: No active interface (0IF): 4 uc LCO; double IF (2IF): 4 uc LTO/2 uc LCO/4 uc LTO; 2IF on LAO substrate: 4 uc LTO/2 uc LCO/4 uc LTO. Top two data sets measured at 10 K, lowermost at 100 K. (b) Spectra from single crystals of model compounds from Ref. [34]. From top to bottom: $EuCoO_3$ (Co^{3+}, LS); Sr_2CoO_3Cl (Co^{3+}, HS); CoO (Co^{2+}, HS system).

location of the two yellow arrows. Now the XAS fingerprint is almost identical to that of CoO: for this double-interface system 100% of the cobalt ions have been transformed into a divalent, d^7 electronic configuration. In the simplest picture this yields a single electron in an otherwise empty e_g orbital manifold. The bottommost trace in Fig. 2(a) (gray) shows that exactly the same result of complete valence transformation occurs also with the LCO under (mild) compressive strain, as this film stack was grown on bulk LAO. Figure S2 of the Supplemental Material [30] shows two methods for decomposing spectra to yield Co^{2+} percentages, and they agree nicely. The effective error in valency determination is of order 5%, leading to an appropriate rounding of all divalent Co percentages in the rest of the paper.

From the data of Fig. 2 it is already clear that the combination of ultrathin LCO sandwiched between LTO does not support regular trivalent cobalt ions, but rather a divalent state, in line with the theory predictions for this couple in Ref. [17]. As each of the Co ions in the 2 uc LCO film has picked up an extra electron, the obvious question arising is, From where? The two main possibilities are the following:

(i) charge transfer of the $3d^1$ electron from the LTO to the cobalt ions (as takes place in the density functional theory (DFT) simulations [17]), or

(ii) a Co valency change as a result of oxygen (or cation) nonstoichiometry in the LCO layer or anionic/cationic intermixing between the layers.

Obviously, this is an important issue to settle. To work out what is happening in these carefully PLD-grown single-, bi-, and trilayer systems with layer thicknesses in the few-uc level in an unbiased manner, a combination of atomic level structural determination and sensitive (and noninvasive) valency determination is required. This is precisely what we bring to bear on the problem using XAS, HAXPES, XPS, and STEM techniques.

As a next step, we discuss data regarding the following:

(i) the range within which the cobalt valency is altered in the LCO (from both XAS and STEM),

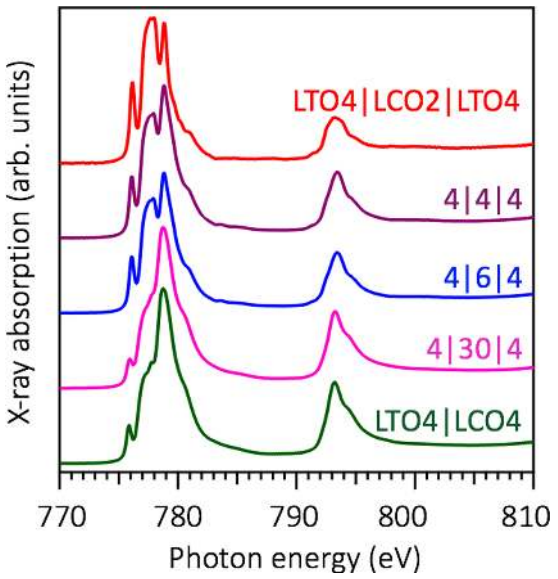

FIG. 3. Interfacial character of charge transfer. Co-$L_{2,3}$ XAS spectra of 2IF systems: 4 uc LTO/x uc LCO/4 uc LTO with $x = 2$, 4, 6, and 36 uc. The bottommost trace from a 1IF 4 uc LTO/2 uc LCO sample shows the 4/36/4 system is similar to the single-IF case. The LCO thickness dependence clearly signals the interfacial character of the electron transfer. All data recorded at 10 K, and individual spectra are offset vertically for clarity.

(ii) the valency of the Ti in the LTO (from XAS and XPS), and

(iii) the crystalline quality of the interfacial systems (from STEM).

For each set of data, we discuss the pros and cons for an explanation via charge transfer from LTO to LCO or via some degree of overoxidation (underoxidation) of the LTO (LCO). This approach allows the reader to form their own opinion of the relative importance of O-2p band alignment and oxygen vacancy effects in this system. At the close of the paper, we will gather together all the arguments, once all the different experimental results have been presented.

We now move to the range in the LCO over which this charge transfer effect is active. This can be probed by varying the LCO thickness in a 4 uc LTO/x uc LCO/4 uc LTO sandwich configuration. The Co-$L_{2,3}$ XAS valency fingerprints for these systems are shown in Fig. 3 for $x = 2$, 4, 6, and 36 uc together with a trace from a single-interface (1IF) 4 uc LTO/4 uc LCO sample for comparison [36].

Starting from the bottom of the stack of spectra in Fig. 3: The 1IF data in green already show the presence of significant divalent cobalt (model compound fits yield 30% divalent Co), linked to a single active LTO/LCO interface.

Next up in Fig. 3 is the 2IF system shown in pink. Here the lowermost interface has been placed 15 nm below the film surface, and thus is essentially invisible in TEY-XAS due to its limited probing depth [27]. Thus, as regards the information depth of the experiment, the 4/36/4 sample should resemble a 1IF system, as the data of Fig. 3 show it does. This is a first indication for interfacial character of the charge transfer.

Moving to the centermost XAS spectrum, confining only 6 uc of LCO between the LTO (blue) brings both interfaces within measurement range, and the result is an increase to 40% divalent Co. As the central LCO layer gets thinner, the average divalent percentage increases: in the 4/4/4 sample half the Co ions are divalent, and as discussed in the context of Fig. 2(a), for 4/2/4 all the trivalent cobalt ions have received an additional electron, turning them divalent.

The deepest-lying LTO/LCO interfaces for $x = 6$, 4, and 2 vary from 5.7 to 4.9 to 4.2 nm below the sample surface, so it is a combination of the reduction of the distance in the LCO to the nearest active LTO/LCO interface and the limited range away from the LTO interface at which the charge transfer into the LCO is effective that are responsible for the strong growth in the overall divalent character.

These LCO-thickness-dependent data on trilayers also are in line with interfacial character of the Co valence transformation. The Co-$L_{2,3}$ XAS data from these trilayers suggest that each interface leads to a remarkably large transformation of the Co valence in the abutting LCO, equivalent to one additional electron in the LCO. In order to correctly interpret the origin of the electrons picked up by the Co ions, atomic-scale information is required on the structure and chemical makeup of the interfacial region.

B. STEM and STEM-EELS data

This brings us naturally to the STEM data. Figure 4(a) shows a HAADF STEM image from a cross section of an LNO-capped LTO4/LCO36/LTO4 film stack grown on STO (substrate not shown). This particular sample was chosen as the upper and lower LTO/LCO interfaces were readily identifiable after focused ion beam based cross-section preparation. From the image, the high quality of the samples is evident.

A 2D representation of the STEM-EELS spatial line-scan data across the two active IFs of the sample is depicted at the Co-L_3 and O-K edges in Figs. 4(b) and 4(c), respectively. These 2D spatial/spectroscopic maps show a definite shifting of the energies of the low-energy features of both the Co-L_3 edge (downward) and the O-K edge (upward) that take place inside the LCO, within ∼3 uc of the LTO/LCO interface. A glance at Figs. 2 and 3 suffices to show that the downward shift observed in the Co-$L_{2,3}$ STEM-EELS data matches the spectral fingerprint of the divalent cobalt seen in XAS. Importantly, the STEM data show that in this 36 uc LCO film, the Co valence transformation takes place within a region within ∼3 uc of interface to the LTO. Thus on a qualitative level, the picture of electron-rich LCO near the LTO interface suggested from the data of Fig. 3 is borne out in the STEM data.

We pause here in the data presentation to point out that the STEM data rule out prominent cationic nonstoichiometry or migration across the $ABO_3/AB'O_3$ interface. Obviously, A-site cationic migration is a nonissue as La has been used throughout all layers in our heterostructures. For the B site, it would be possible for Ti and Co to migrate across interfaces in both directions and take on different valence states. However, both the HAADF-STEM and the EELS data from multiple samples yield no indication—within the error margins of a single uc—that such migration occurs, nor was significant cation nonstoichiometry observed in either material.

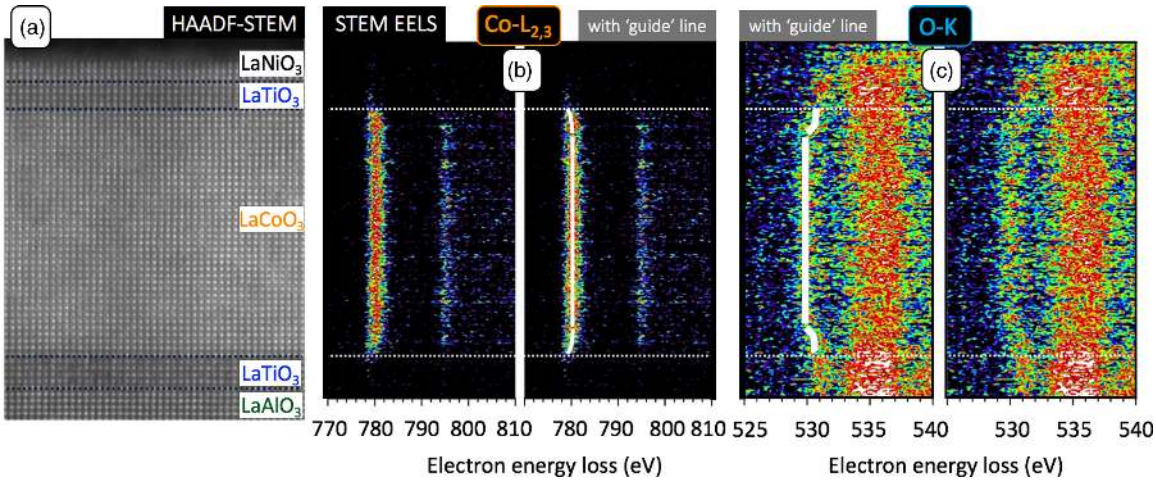

FIG. 4. STEM imaging and spectroscopy. (a) HAADF-STEM cross section showing excellent epitaxy and sharp interfaces. Panels (b) and (c) show STEM-EELS data from the same cross section. In (b) a downshift of the Co-$L_{2,3}$ main feature close to the active IF is consistent with interfacial Co(II). In (c) an upshift of interfacial O-K prepeak in LCO is seen, also consistent with interfacial Co(II). In the central images of (b) and (c) the white lines schematically indicate the energy shifts occurring. All data recorded at room temperature and in the 2 T field of the objective lens.

At this stage, it is useful to turn to the electronic states and valency of the Ti in the LTO in these heterostructures, which can be measured using core level photoemission and XAS. In Fig. S3 of the Supplemental Material [30], the Ti-$L_{2,3}$ edges of the LTO layers in 2IF samples composed of 2, 4, and 6 uc of LCO between a pair of 4 uc LTO layers are shown, as well as those of STO. The intensity ratio of the first two (L_3, t_{2g}, and e_g related) structures are different in the trilayers compared to STO, but otherwise all four traces clearly signal Ti in the tetravalent ($3d^0$) state. On a *qualitative* level this can argue for the transfer of the $3d$ electron of the LTO to LCO, as predicted in [17]. However, on a charge-counting level the data reveal that more electrons are lost from Ti than are gained by Co. The $4/2/4$ sample is the clearest example of this: 2 uc of LCO have a $3d^7$ (divalent) configuration, as shown in the data of Fig. 2, yet Fig. S3 shows that 8 uc of LTO are in a $3d^0$ initial-state configuration. This fact immediately means that the interpretive slider on a scale from—on the one hand—(a) O-$2p$ alignment driven charge transfer between stoichiometric LTO and LCO and—on the other hand—(b) oxygen nonstoichiometry induced valence changes (in both LTO and LCO) cannot lie fully at the "(a) only" end of the scale. This conclusion is only natural, given the intermediate oxygen pressure in which we chose to grow the samples: one could expect the formation of $LaTiO_{3+\delta}$ and $LaCoO_{3-\delta}$, as this has been seen in the growth of each material as a "stand-alone" system [19,25]. We do mention here that the XAS traces from reference LCO films grown under identical conditions to the LCO in the bi- and trilayers show divalent Co only at the $<3\%$ level, which would obviously not explain the high percentages of divalent Co in the heterostructures.

Returning to the LTO, in Fig. S4 of the Supplemental Material [30] we use *in situ* XPS experiments to show that the Ti valence in an LTO film grown on LAO under the conditions given in Table I, and then transferred without breaking vacuum from the PLD to the XPS system, can be altered between essentially tetravalent to majority trivalent, depending on a UHV annealing protocol. These valency changes would be in line with the LTO overoxidation phenomena reported in Ref. [19]. From a solid-state chemistry point of view, the extra oxygen interstitials required to remove 6 Ti-$3d$ electrons (2 electrons being hosted by the LCO layer) from the 2×4 uc of LTO in the $4/2/4$ trilayer sample are not an easy "fit" in a space-filling representation of the 113-ABO_3 structure for the LTO and should result in some degree of structural deformation. Indeed, in $LaTiO_{3+\delta}$ with Ti^{4+}, one could expect to see line defects belonging to the 227 phase [24], which we do not see in the STEM data. Analogously, if oxygen vacancies in LCO account for the presence of the entirely divalent Co population in the $4/2/4$, the result would be the formation of the brownmillerite structure $LaCoO_{2.5}$ [37] in the central LCO block, something not supported by the STEM data presented here. Nevertheless, the XPS experiments of Fig. S4 do show alterations in Ti valence in our LTO films and this should also find a place in the interpretative framework for the data from the bi- and trilayer systems.

In addition to the issue of the true electron count in the LTO structures, the Ni-$3d$ level in the LNO cap could act as an acceptor for electrons from the LTO, or indeed from the LCO. LNO was not covered as an example in the DFT data of Ref. [17], and the use of LNO (chosen to avoid A-site migration issues) means there is a strong overlap of the La-$M_{4,5}$ lines with the Ni-$L_{2,3}$ features thus complicating Ni valence determination in XAS of the LNO layer. Consequently, both the electron-counting imbalance mentioned above and the smaller divalent Co contribution seen in thin, 1IF samples relative to the expectation from the 3 uc charge transfer range from STEM could have a connection to the LNO. We freely admit that this is a potential complication; however, as mentioned in the introduction, a cap was included to minimize the effects of atmospheric exposure and LNO was found to be a good candidate to enable charging-free, low-temperature TEY measurements.

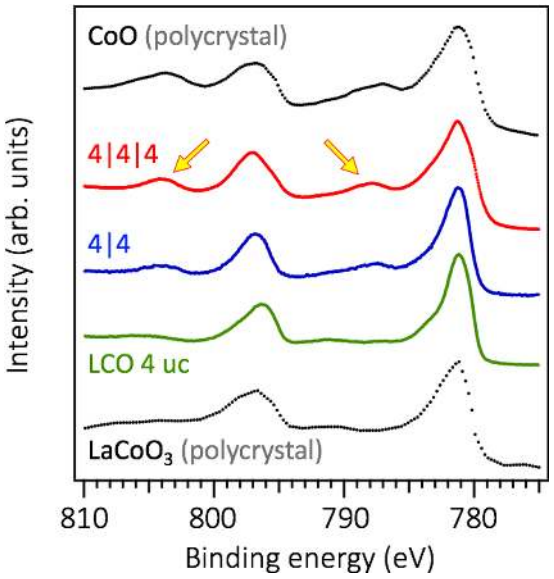

FIG. 5. XPS confirms Co(III)-d^7 ions in interface samples: HAXPES spectra of the Co-2p core level of (top to bottom) CoO (Ref. [44]); 2IF LTO4/LCO4/LTO4 and 1IF LTO4/LCO4 on LAO substrates and LCO 4 uc on a Nb:STO substrate (red, blue, and green, respectively); and bulk LCO (Ref. [21]). The thin-film data were recorded using $h\nu = 2.2$ keV at 250 K, and the yellow arrows highlight the shake-up satellites characteristic of octahedrally coordinated Co(II) ions. Individual spectra are offset vertically for clarity.

Returning to the STEM data, we see a clean perovskite structure throughout the whole stack for all types of samples that we have presented in this paper. For example, ordered defects have already been seen experimentally for 10% oxygen vacancies, equivalent to a composition of $LaCoO_{2.7}$ [38]. Our STEM data are wholly devoid of the stripe- or line-like features that have been interpreted in the literature as Co spin-state ordering or O-vacancy ordering in LCO [38–42]. In epitaxial films one would also expect a measurable expansion of the LCO c-lattice parameter [43], something which is not seen in our STEM data. Ion milling to generate (S)TEM samples is ubiquitous, and also used in Ref. [38], which saw ordered vacancies in LCO. Thus, although milling-induced or STEM beam-induced alterations of the oxygen content cannot be excluded, the agreement between our XAS and STEM-EELS data suggests that ion-milling damage is not a leading-order factor in the data presented here.

C. HAXPES and XPS data

Figure 5 shows Co-2p HAXPES spectra of a 0IF 4 uc LCO sample (Nb:STO substrate), 1IF 4 uc LTO/4 uc LCO, and 2IF 4 uc LTO/4 uc LCO/4 uc LTO, the latter grown on LAO substrates, together with reference spectra from bulk LCO and CoO from the literature [21,44]. The Co-2p photoemission line shape is a result of numerous final-state charge-transfer and multiplet interactions and this cautions against a strict quantitative analysis. However, the absence or presence of characteristic satellite structures appearing at ~6 eV higher binding energy than the main spin-orbit-split main lines is a telltale sign of the Co valence. These features are indicated in Fig. 5 using yellow arrows, and are a result of a so-called "shake-up" process in which ligand-to-metal charge transfer takes place, yielding a $|2p^5 3d^{n+1}\underline{L}\rangle$ final state [45]. In octahedrally coordinated Co(III) systems such as bulk LCO, the charge transfer energy, Δ, required to do this is too great and no satellite is observed [46], but in divalent Co(II) this is a salient feature of the spectrum [47].

Looking at the data of Fig. 5, it is clear that the 1IF 4/4 sample shows clear satellite intensity [and thus presence of Co(II) ions] and that this increases further in the case of the 2IF 4/4/4 sample, following the same trend as seen in the XAS data. In line with this, for the 4 uc LCO film without an "active" LTO/LCO interface, no shake-up satellite is observable, just as for the bulk LCO spectrum from trivalent cobalt. Given the thinness of the cobaltate layers and the significant inelastic mean-free path length of the photoelectrons under these conditions, no depth profiles could be extracted from the angle-dependent HAXPES data.

D. Testing the range of charge transfer

This penultimate results section of the paper presents a double-check of the range over which the charge transfer between LTO and LCO is active. The calculations of Ref. [17] also suggested the possibility of modulation doping, in which there is spatial separation between the location of the (potential) conduction electrons and the dopants/structures that give rise to the charge transfer. Up to 5 uc of a transition metal oxide $SrZrO_3$ buffer layer (what we call below a "break" layer) is suggested to be able to leave the interfacial charge transfer unaffected [17]. Given the very robust dependability of the PLD growth, growth of samples including such "break" layers provides a simple, combined test of both the interfacial nature of the charge transfer and the practical feasibility of modulation doping in such oxide heterostructures.

In Fig. 6 the main Co-L_3 XAS feature is shown for a series of 1IF samples. The LTO4/LCO4 (red) and LCO4 (blue) have been discussed before, with the former showing 25% divalent Co and the latter <3%. The three traces in between possess a single IF, but with a varying number (here 1, 2, and 8) of unit cells of LAO slipped in between as an electronic break layer [see Fig. 1(d)]. As LAO is a wide band gap insulator, with no variable oxidation state cations, it is a highly effective charge transfer circuit breaker. The inset highlights the lowest energy divalent Co prepeak feature, and clearly shows what is happening: charge transfer at a level comparable to that in the LTO4/LCO4 system is maintained despite addition of a single uc of LAO as a break. However, already an LAO break of only 2 uc reduces the telltale divalent Co feature by a factor 2.5.

In the context of the LAO/STO interface possessing a 2D electron gas in the STO, the inclusion of a $SrCuO_2$ layer as an oxide ion supplier above 10 uc of LAO on STO removed the thermally activated defect donor states at the STO interface, boosting the mobility fivefold [48]. The success of this sample design involving the cuprate layer shows that oxide ions can be effectively transmitted by LAO over even 10 uc thicknesses. Thus, if the divalent Co seen in the bi- and trilayer samples were to be dominantly due to oxygen gettering by the

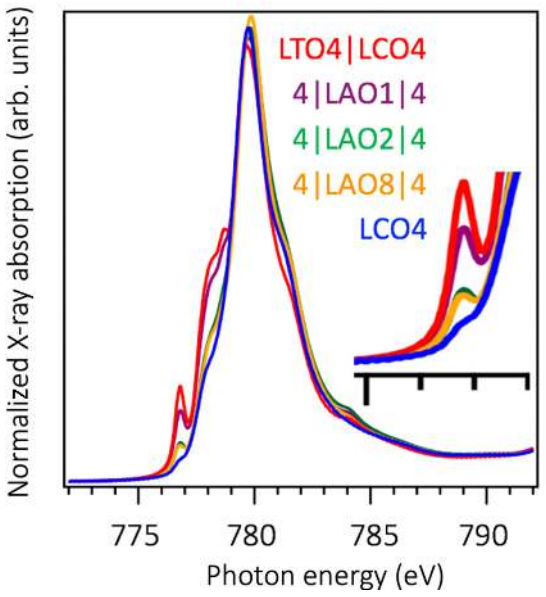

FIG. 6. Testing "modulation doping" style charge transfer idea using LAO "break" layers: Co-L_3 XAS traces of 4 uc LTO/x uc LAO/4 uc LCO, with $x = 0$, 1, 2, 8. LAO interrupts the charge transfer, approaching the zero-active-IF 4 uc LCO system. The inset shows a zoom of the prepeak region.

LTO from the LCO, given the proven transmission of oxide ions through LAO [48], the strong reduction in divalent Co for the break-layer samples with LAO thicknesses of 2 and 8 uc would be hard to understand. However, if the divalent Co results from O-2p band alignment driven interfacial charge transfer, then the data of Fig. 6 would seem to confirm the DFT-based expectation that the charge transfer can bridge a thin insulating barrier.

E. XMCD data and sum rule analysis

In the final results part of the paper, we turn to the spin state and magnetic properties of the Co ions in the LCO films. Obviously, there is no straightforward manner in which the individual Co(II) ions with Co-3d^7 configuration can be spinless. Measuring the magnetic properties of complex oxides in the form of ultrathin films as components in heterostructures on bulk substrates is a severe technical challenge for regular magnetometry. In such cases, the chemical specificity offered by XMCD [49,50] offers not only exquisite sensitivity, but also—via application of XMCD sum rules [51]—extraction of both the spin and orbital moments.

Panels (a)–(d) of Fig. 7 show XMCD data recorded in different applied magnetic fields for 0IF, 1IF, and 2IF systems. Figure S5 of the Supplemental Material [30] shows exemplary raw σ^+ and σ^- XAS data that yield the XMCD signal. Each XMCD panel in Fig. 7 is on the same y scale in units of the percentage of the maximal Co-L_3 absorption. As is expected for a thin-film system [22], the 0IF 4 uc LCO sample is not perfectly low spin, with the data of Fig. 7 showing an XMCD signal at the 7–8 percent level at the maximal field of 14 T. Adding an active LTO/LCO interface (1IF: LTO4/LCO4) alters the spectral form of the XMCD signal and it more than doubles in magnitude. Upon going to the 2IF systems LTO4/LCO4/LTO4 and LTO4/LCO2/LTO4, the XMCD signal is four- and sixfold enhanced compared to that of the single LCO layer. Thus, it is very clear that the controlled charge transfer between LTO and LCO is turning the interfacial cobalt ions into magnetically polarizable entities,

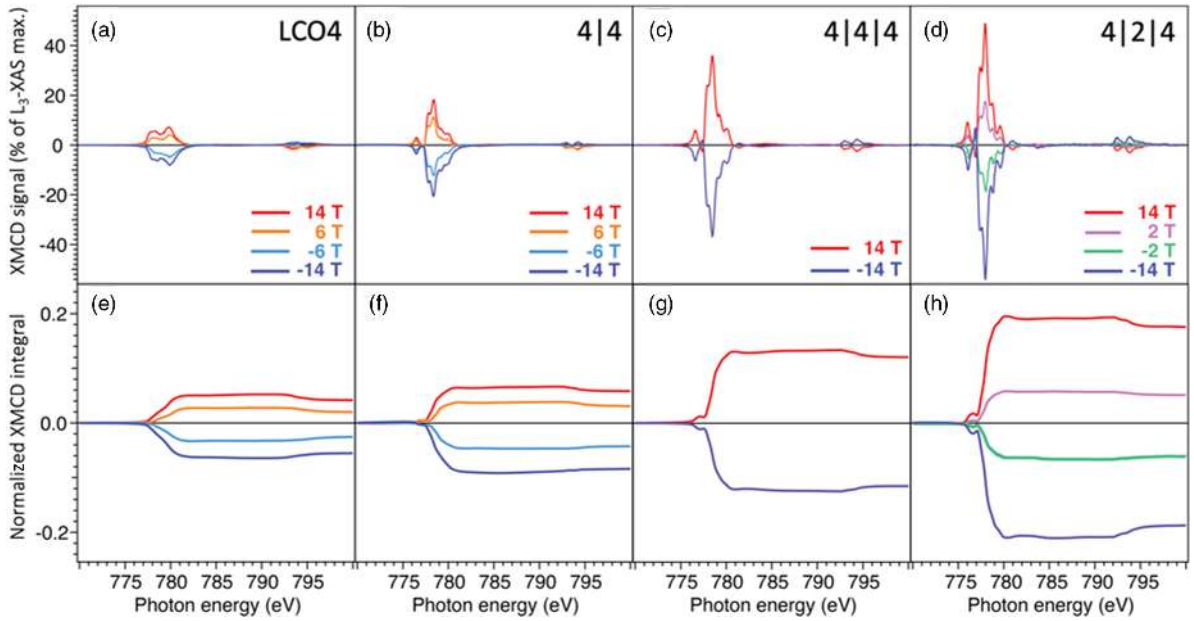

FIG. 7. XMCD shows boosted Co magnetic moment on formation of Co(III)-d^7 ions in interface samples: (a)–(d) TEY-XMCD signal (σ^+-σ^-) at the Co-$L_{2,3}$ edges as a percentage of the maximum of the Co-L_3 absorption. Panels (e)–(h) show the integrals over the XMCD signals, normalized to the integral of the unpolarized absorption for the same data. Panels (a), (e) are for 0IF: 4 uc LCO; (b), (f) are for 1IF: 4 uc LTO/4 uc LCO; (c), (g) are for 2IF: 4 uc LTO/4 uc LCO/4 uc LTO; (d), (h) are for 2IF: 4 uc LTO/2 uc LCO/4 uc LTO. All data are measured at 10 K with the samples cooled in the fields shown.

TABLE II. Magnetic parameters from XMCD sum rule analysis for −14 T applied field at 10 K.

System	Percent Co(II) from XAS	Orbital moment m_l (μ_B) from XMCD	Spin moment m_s (μ_B) from XMCD	m_l/m_s	Total moment m_{tot} (μ_B) from XMCD	Saturation magnetization M_{sat} (μ_B) from Brillouin function	Factor increase in m_{tot} cf. LCO4
0IF LCO4	<3	0.15	0.33	0.45	0.48	0.53	
1IF LTO4/LCO4	25	0.2	0.38	0.55	0.58	0.64	1.2
2IF LTO4/LCO6/LTO4	40	0.26	0.5	0.52	0.76	0.89	1.2
2IF LTO4/LCO4/LTO4	50	0.26	0.47	0.54	0.73	0.81	1.5
2IF LTO4/LCO2/LTO4	100	0.37	0.75	0.50	1.16	1.29	2.4

in keeping with the odd number of electrons in their d shell from the XAS line shape analysis.

The XMCD sum rules enable extraction of more quantitative information on the magnetic properties [50]. These involve the integration of the XMCD signal over the photon energy region of the Co L_2 and L_3 edges, and panels (e)–(h) of Fig. 7 show these normalized XMCD integrals. Already without any further analysis, the fact that the XMCD integral shows a downward step at the L_2 edge and maintains a finite value thereafter indicates that the Co ions possess both spin *and* orbital moments.

The spin and orbital moments extracted from the sum rule analysis are shown in Table II. Increasing the number of active interfaces boosts both the spin and orbital moments by factors equal to or exceeding 1.2 (1IF), 1.5 (2IF with LCO4), and 2.4 (2IF with LCO2) compared to 0IF (LCO4). For all samples, the orbital moment is considerable, amounting to half of the spin moment, and is aligned parallel to the spin moment, meaning the g factor exceeds 2 in these systems.

Grown under coherent epitaxial strain on bulk STO, the LCO layers in these systems are under in-plane tensile strain: $c/a < 1$. Studies of 10 nm thick films of CoO grown either sandwiched between MnO on a Ag substrate or grown directly on silver [52] have shown that the $3d$ spin-orbit interaction prevents the collapse of the orbital moment [53] for high-spin Co-$3d^7$ states when $c/a < 1$. We propose that this same mechanism is likely to be operative in the in-plane tensile-strained LCO films presented here.

The data presented in Fig. 7 and their analysis clearly point to the generation of spinful Co-$3d^7$ entities as soon as one or more active LTO/LCO interfaces are introduced, with a total moment of 1.16 μ_B, and m_l/m_s of 0.5 for the fully divalent cobalt ions in LTO4/LCO2/LTO4.

In order to discuss the magnetic behavior of the Co ions, Fig. 8 presents the field and temperature dependence of the magnetization extracted from the XMCD sum rules for a 0IF LCO sample and two 2IF systems: LTO4/LCO6/LTO4 and LTO4/LCO2/LTO4. The color-coded solid lines are fits to $M = M_{sat}B_J(x)$, where the experimentally determined m_l/m_s ratio and the S expected from the valence observed in the XAS were used to calculate J using a Brillouin function

$$B_J(x) = \frac{2J+1}{2J}\coth\left[\frac{(2J+1)x}{2J}\right] - \frac{1}{2J}\coth\left(\frac{x}{2J}\right),$$

$$\text{with} \quad x = \frac{g_J\mu_B JB}{k_BT}.$$

The Landé g value is

$$g_J = \frac{3}{2} + \frac{S(S+1) - L(L+1)}{2J(J+1)},$$

and we note that such a Brillouin function describes the spin physics of a collection of spins behaving paramagnetically [54].

The saturation magnetization, M_{sat}, was varied to achieve optimal fits to the experimental field dependence (main figure) or T dependence (inset) of the data. M_{sat} is about 10% greater than the values connected to maximal (minimal) fields (temperatures) accessed experimentally. Simple inspection of Fig. 8 shows the Brillouin function captures the essence of the

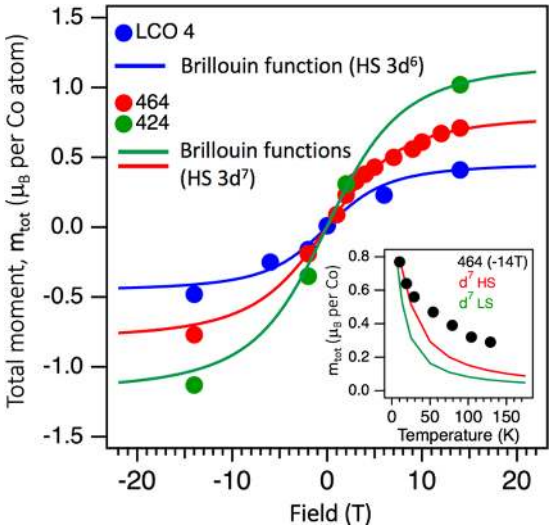

FIG. 8. Magnetic field and temperature dependence of the cobalt element-specific magnetization shows Brillouin function behavior. Shown is the field dependence of m_{tot}, the sum of spin and orbital moments (colored symbols), determined using the XMCD sum rules for 0IF: 4 uc LCO (blue), and 2IF: 4 uc LTO/6 uc LCO/4 uc LTO (red) and 4 uc LTO/2 uc LCO/4 uc LTO (green). The solid lines show fits using a Brillouin function ($T_{sample} = 10$ K) for S values from the XAS valence analysis ($S = 3/2$ for HS Co $3d^7$; $S = 2$ for HS Co $3d^6$) and L values matching the determined m_l/m_s values from the sum rules. The inset shows the temperature dependence of the sum of spin and orbital moments for the 2IF system 4 uc LTO/6 uc LCO/4 uc LTO (black symbols) measured in a field of −14 T. The lines show the Brillouin function behavior expected for HS Co $3d^7$ HS (red) and LS Co $3d^7$ (green).

field dependence and the strong decay of the magnetization as temperature is raised for all the samples measured, indicating paramagnetic behavior.

For the 0IF system LCO4, the $3d^6$ HS ($S = 2$) population provides the paramagnetic magnetic response [55], and taking into account the experimentally determined m_l/m_s ratio of 0.45, a good fit is achieved for a saturation magnetization of $M_{\rm sat}(\rm LCO4) = 0.45\mu_B$ per Co atom.

For the 2IF systems LTO4/LCO6/LTO4 and LTO4/LCO2/LTO4, in which charge transfer has created divalent Co-$3d^7$ ions, there are two options:

(i) a high-spin $t_{2g}^5 e_g^2$ $S = 3/2$ state (HS), or

(ii) a low-spin $t_{2g}^6 e_g^1$ $S = 1/2$ state (LS).

The Brillouin function fits in the main panel of Fig. 8 are for HS $3d^7$, the same spin state as in CoO (the latter is also HS as a thin film under either compressive or tensile in-plane strain [52]). Without exception, divalent cobalt oxides are quoted as HS in the literature, as their on-site Coulomb interaction energy U_{dd} (at the root of Hund's first rule) is greater that the crystal field energy. In the mixed-valent cobalt oxide $La_{1.5}Sr_{0.5}CoO_4$, successful modeling of the Co-$L_{2,3}$ XAS using a combination of the spectra from $EuCoO_3$ (LS Co $3d^6$) and CoO (HS Co $3d^7$) is provided as evidence that the divalent Co in $La_{1.5}Sr_{0.5}CoO_4$ is HS [56]. The fact that the XAS data from our bi- and trilayer samples can also be fitted in exactly the same way (see Fig. S2) argues by analogy for the conventional HS spin state for the divalent Co $3d^7$ here. Having said that, the Brillouin function fit for the field dependence for the LS $3d^7$ state only gives a marginally worse fit. The saturation magnetizations—using m_l/m_s ratios of 0.52 for both 2IF samples—are $0.89\mu_B$ and $1.29\mu_B$ per Co atom for LTO4/LCO6/LTO4 and LTO4/LCO2/LTO4, respectively, as shown in Table II.

The expected spin-only magnetic moment in a simple single-ion picture for HS Co $3d^7$ would be $3\mu_B$ per Co, and under similar assumptions would be $1\mu_B$ for LS Co $3d^7$. In this straightforward view, the LS configuration can be argued to yield a spin moment closer to the experimental spin-only value of $0.75\mu_B$ for the fully Co-$3d^7$ LTO4/LCO2/LTO4 system. Arguments can also be made that the improved Goldschmidt tolerance factor for the smaller LS Co-$3d^7$ ion [57] of ($t = 0.958$) compared to the HS one ($t = 0.915$) could also help counteract the additional Coulomb repulsion cost of the LS state.

The inset to Fig. 8 shows the temperature dependence of total magnetic moment of the 2IF system LTO4/LCO6/LTO4 in the range of 10 to 180 K. Example XMCD spectra underlying the data points of Fig. 8 are shown in Fig. S6(a) of the Supplemental Material [30]. The solid lines are from the Brillouin functions (red: HS $3d^7$, $S = 3/2$, $m_l/m_s = 0.53$; green: $3d^7$ LS, $S = 1/2$, $m_l/m_s = 0.53$) with $M_{\rm sat} = 0.89\mu_B$. The high-spin curve yields a better result than for the LS state. Both fit curves show steeper decay of the magnetization than do the data, and suggest a contribution to the experimental value of the total moment from another source that grows as temperature is raised. A natural candidate for this is a trivalent Co-$3d^6$ HS contribution ($S = 2$) growing from zero at 10 K to of order 15% at 150 K [22]. Given that 60% of the Co in the LTO4/LCO6/LTO4 system for which we have the detailed field- and temperature-dependent XMCD data is simply trivalent LCO, it is not unreasonable to suggest that this is the source of the additional magnetization at higher temperatures.

In any case, the lack of remnant magnetization in zero field, and the good description provided by the Brillouin function at low temperatures argues firmly against ferromagnetism in the case of these bi- and trilayer interfacial Co spin systems [58]. In keeping with this, Fig. S6(b) of the Supplemental Material [30] shows a lack of in-plane/out-of-plane anisotropy in the XMCD of the 2IF system LTO4/LCO4/LTO4. It is also clear from Fig. 8 that these interfacial systems are not generating a long-range-ordered antiferromagnetic (AFM) ground state. AFM Co-Co correlations, however, have been cited as the cause of reduced moments for the paramagnetic, divalent Co sites in FM films of Co-doped ZnO studied using XMCD [59], and in thick, Ce-doped LCO films (also containing HS Co $3d^7$), reduced moments are also reported [60]. Thus, AFM correlations or local patches of AFM order could be responsible for the reduced saturation magnetization of the Co $3d^7$ ions from the XMCD analysis on these bi- and trilayers. Detailed angular- and T-dependent x-ray magnetic linear dichroism measurements would be required to examine possible (incipient) AFM ordering while distinguishing these magnetic contributions from charge order/anisotropies in these noncubic systems [61]. Such experiments go well beyond the remit of this investigation.

The bottom line of the XMCD experiments on the magnetic properties is that the interfacial charge transfer clearly increases the spin and orbital moments, with the Co $3d^7$ spins displaying paramagnetic behavior.

The rich spin physics of cobalt oxides also sheds light on the lack of electrical conduction in these systems, also for cases with noninteger $3d$ electron counts. If the divalent Co $3d^7$ are in a HS state and neighboring trivalent Co $3d^6$ are low spin, then a process called spin blockade prohibits hopping, suppressing conduction, as has been suggested in $HoBaCo_2O_{5.5}$ [62], $La_{1.5}Sr_{0.5}CoO_4$ [56], and Ce-doped LCO films [60]. For the $3d^7$ integer electron count in the 2IF 4 uc LTO/2 uc LCO/4 uc LTO system, Mott physics most likely lies at the root of the insulating ground state.

Before concluding, we return to the key discussion of the microscopic origin of the remarkable charge transfer to create structurally unaltered, paramagnetically polarizable Co^{2+} at a 100% level across all LCO unit cells abutting LTO in high-quality, nonpolar oxide heterointerfaces. The data are very clear in that the Ti of the LTO is $3d^0$ and the Co of the LCO is $3d^7$ (divalent), supporting the DFT prediction that the LCO/LTO couple exists as $3d^7/3d^0$ and not $3d^6/3d^1$.

Electronic charge transfer and oxygen migration between the LCO and LTO (oxygen "gettering" by the LTO) are the two frontrunner mechanisms for the observed behavior, as both are sensitive to the number of active LTO/LCO interfaces present in the sample. Some aspects of the experimental data point to oxygen nonstoichiometry in the LTO, yet others argue against oxygen-gettering effects between the layers as being dominant. In reality, a combination of these two mechanisms is most likely at work, so as to avoid the $3d^6/3d^1$ situation when interfacing LCO and LTO. Here we reiterate the key experimental data relevant to the oxygen-gettering discussion:

(i) The addition of an oxide-ion-permeable LAO break layer between LTO and LCO strongly suppresses the formation of divalent Co, arguing against oxygen gettering by LTO from LCO as the dominating factor.

(ii) The STEM data show that the altered Co valence is localized close to the LCO/LTO interface and that no oxygen vacancy ordering is present at sufficient density in the LCO to explain the Co valence. The STEM data also do not show structural alterations such as line defects associated with crystalline domains of $La_2Ti_2O_7$ in the LTO or brownmillerite $LaCoO_{2.5}$ in the LCO.

(iii) Nevertheless, charge counting in the trilayers (such as the 4/2/4 and 4/4/4 systems) shows that more charge is lost from LTO than is gained by LCO. This would appear to signal overoxidation of the LTO, something possible due to the relatively high oxygen partial pressure in the growth step, without the need for the LTO to getter oxygen from the LCO layer. The mechanism of overoxidation remains unclear and should be the subject of further investigation.

(iv) Electron transfer from the LTO to the LNO cap cannot be excluded as an additional channel by which a Ti-$3d^0$ configuration in reached in the LTO.

VI. CONCLUSIONS AND OUTLOOK

We have grown high-quality thin films of the charge transfer insulator LCO using PLD possessing either 0, 1, or 2 structurally abrupt, nonpolar interfaces to the Mott insulator LTO. The data clearly show that the O-2p band alignment based DFT prediction of a Co-$3d^7$/Ti-$3d^0$ electronic configuration is correct. The heterointerface, although nonconducting due to spin blockade physics for noninteger average charge states, provides a controllable population of interfacial, most likely HS, divalent Co.

The magnitude of the electron transfer for the bi- and trilayers is one electron per interfacial LTO/LCO uc, per interface in the structure. Therefore, the LCO film thickness and the number of LTO/LCO interfaces provide a pair of deterministic control knobs for the average valency of the LCO layer. Overoxidation of the LTO layer also plays a role in determining the Ti valence, yet the reduction in divalent Co signals via insertion of an oxide-ion-permeable yet electrically insulating "break" layer between the LTO and LCO points toward the charge transfer mechanism predicted in the DFT calculations. The interfacial $3d^7$ Co ions formed by charge transfer exhibit significant orbital moment, likely due to a combination of the anisotropic crystal field and Co-3d spin-orbit coupling, and detailed XMCD investigations point clearly to their paramagnetic behavior.

These experiments clearly affirm the O-2p band alignment concept as a successful design philosophy for the engineering of strongly correlated quantum materials [17], without the need for the system to be responding to an incipient polar catastrophe, and without introducing cationic disorder connected to chemical doping. To be able to do this is of interest in controlling conductivity, magnetic states, and also (catalytic) chemical reactivity.

ACKNOWLEDGMENTS

This research is part of the NWO/FOM research program DESCO (VP149), which is financed by the Nederlandse Organisatie voor Wetenschappelijk Onderzoek (NWO). D.K., J.V., and N.G. acknowledge funding from the *Geconcentreerde Onderzoekacties* (GOA) project "Solarpaint" of the University of Antwerp. The Qu-Ant-EM microscope used in this study was partly funded by the Hercules Fund from the Flemish Government. The authors are grateful to David McCue, Mark Sussmuth, and Paul Steadman at Diamond Light Source for excellent user support. The synchrotron-based experiments have been supported by the project CALIPSOplus under Grant Agreement No. 730872 from the EU Framework Programme for Research and Innovation HORIZON 2020. S.K.M. thanks the Department of Science and Technology, India (SR/NM/Z-07/2015), for financial support, and Jawaharlal Nehru Centre for Advanced Scientific Research (JNCASR) for managing the project.

M.S.G., G.A.K., J.G., and G.K. conceived and planned the XAS and HAXPES experiments. J.G., G.K., and G.R. synthesized the samples and performed lab XPS and data analysis. M.S.G., G.A.K., J.G., S.K.M., S.S., and X.V. carried out the synchrotron work, with the data analysis done by G.A.K. and M.S.G., while P.B., T.-L.L., and C.S. provided essential user support at the synchrotron. N.G., D.K., J.F., and J.V. carried out TEM-EELS experiments and their analysis. M.S.G. and G.A.K. wrote the manuscript and all authors contributed to the discussion and revision of the manuscript.

[1] K. Mizushima, P. C. Jones, P. J. Wiseman, and J. B. Goodenough, Li_xCoO_2 ($0 < x < -1$): A new cathode material for batteries of high energy density, Mater. Res. Bull. **15**, 783 (1980).

[2] F. S. Foster, C. J. Pavlin, K. A. Harasiewicz, D. A. Christopher, and D. H. Turnbull, Advances in ultrasound biomicroscopy, Ultrasound Med. Biol. **26**, 1 (2000).

[3] T. R. Shrout and S. J. Zhang, Lead-free piezoelectric ceramics: Alternatives for PZT?, J. Electroceram. **19**, 113 (2007).

[4] M. Imada, A. Fujimori, and Y. Tokura, Metal-insulator transitions, Rev. Mod. Phys. **70**, 1039 (1998).

[5] Y. Tokura and N. Nagaosa, Orbital physics in transition-metal oxides, Science **288**, 462 (2000).

[6] A. Ohtomo and H. Y. Hwang, A high-mobility electron gas at the $LaAlO_3/SrTiO_3$ heterointerface, Nature (London) **427**, 423 (2004).

[7] A. Brinkman, M. Huijben, M. van Zalk, J. Huijben, U. Zeitler, J. C. Maan, W. G. van der Wiel, G. Rijnders, D. H. A. Blank, and H. Hilgenkamp, Magnetic effects at the interface between non-magnetic oxides, Nat. Mater. **6**, 493 (2007).

[8] N. Reyren, S. Thiel, A. D. Caviglia, L. F. Kourkoutis, G. Hammerl, C. Richter, C. W. Schneider, T. Kopp, A.-S. Ruetschi, D. Jaccard, M. Gabay, D. A. Muller, J.-M. Triscone, and J. Mannhart, Superconducting interfaces between insulating oxides, Science **317**, 1196 (2007).

[9] A. D. Caviglia, S. Gariglio, N. Reyren, D. Jaccard, T. Schneider, M. Gabay, S. Thiel, G. Hammerl, J. Mannhart, and J.-M. Triscone, Electric field control of the $LaAlO_3/SrTiO_3$ interface ground state, Nature (London) **456**, 624 (2008).

[10] N. Nakagawa, H. Y. Hwang, and D. A. Muller, Why some interfaces cannot be sharp, Nat. Mater. **5**, 204 (2006).

[11] A. Kalabukhov, R. Gunnarsson, J. Börjesson, E. Olsson, T. Claeson, and D. Winkler, Effect of oxygen vacancies in the $SrTiO_3$ substrate on the electrical properties of the $LaAlO_3/SrTiO_3$ interface, Phys. Rev. B **75**, 121404(R) (2007).

[12] S. A. Chambers, L. Qiao, T. C. Droubay, T. C. Kaspar, B. W. Arey, and P. V. Sushko, Band Alignment, Built-In Potential, and the Absence of Conductivity at the $LaCrO_3/SrTiO_3(001)$ Heterojunction, Phys. Rev. Lett. **107**, 206802 (2011).

[13] E. Slooten, Z. Zhong, H. J. A. Molegraaf, P. D. Eerkes, S. de Jong, F. Massee, E. van Heumen, M. K. Kruize, S. Wenderich, J. E. Kleibeuker, M. Gorgoi, H. Hilgenkamp, A. Brinkman, M. Huijben, G. Rijnders, D. H. A. Blank, G. Koster, P. J. Kelly, and M. S. Golden, Hard x-ray photoemission and density functional theory study of the internal electric field in $SrTiO_3/LaAlO_3$ oxide heterostructures, Phys. Rev. B **87**, 085128 (2013).

[14] Z. Liao, M. Huijben, Z. Zhong, N. Gauquelin, S. Macke, R. J. Green, S. van Aert, J. Verbeeck, G. van Tendeloo, K. Held, G. A. Sawatzky, G. Koster, and G. Rijnders, Controlled lateral anisotropy in correlated manganite heterostructures by interface-engineered oxygen octahedral coupling, Nat. Mater. **15**, 425 (2016).

[15] P. Zubko, S. Gariglio, M. Gabay, P. Ghosez, and J.-M. Triscone, Interface physics in complex oxide heterostructures, Annu. Rev. Condens. Matter Phys. **2**, 141 (2011).

[16] H. Kroemer, Nobel lecture: Quasielectric fields and band offsets: Teaching electrons new tricks, Rev. Mod. Phys. **73**, 783 (2001).

[17] Z. Zhong and P. Hansmann, Band Alignment and Charge Transfer in Complex Oxide Interfaces, Phys. Rev. X **7**, 011023 (2017).

[18] J. E. Kleibeuker, Z. Zhong, H. Nishikawa, J. Gabel, A. Müller, F. Pfaff, M. Sing, K. Held, R. Claessen, G. Koster, and G. Rijnders, Electronic Reconstruction at the Isopolar $LaTiO_3/LaFeO_3$ Interface: An X-Ray Photoemission and Density-Functional Theory Study, Phys. Rev. Lett. **113**, 237402 (2014).

[19] P. Scheiderer, M. Schmitt, J. Gabel, M. Zapf, M. Stübinger, P. Schütz, L. Dudy, C. Schlueter, T.-L. Lee, M. Sing, and R. Claessen, Tailoring materials for mottronics: Excess oxygen doping of a prototypical Mott insulator, Adv. Matter. **30**, 1706708 (2018).

[20] J. Suntivich, K. J. May, H. A. Gasteiger, J. B. Goodenough, and Y. Shao-Horn, A perovskite oxide optimized for oxygen evolution catalysis from molecular orbital principles, Science **334**, 1383 (2011).

[21] T. Saitoh, T. Mizokawa, A. Fujimori, and M. Abbate, Electronic structure and temperature-induced paramagnetism in $LaCoO_3$, Phys. Rev. B **55**, 4257 (1997).

[22] M. W. Haverkort, Z. Hu, J. C. Cezar, T. Burnus, H. Hartmann, M. Reuther, C. Zobel, T. Lorenz, A. Tanaka, N. B. Brookes, H. H. Hsieh, H.-J. Lin, C. T. Chen, and L. H. Tjeng, Spin State Transition in $LaCoO_3$ Studied Using Soft X-Ray Absorption Spectroscopy and Magnetic Circular Dichroism, Phys. Rev. Lett. **97**, 176405 (2006).

[23] G. Koster, G. Rijnders, D. H. A. Blank, and H. Rogalla, Surface morphology determined by (001) single crystal $SrTiO_3$ termination, Phys. C (Amsterdam) **339**, 215 (2000).

[24] A. Ohtomo, D. A. Muller, J. L. Grazul, and H. Y. Hwang, Epitaxial growth and electronic structure of $LaTiO_x$ films, Appl. Phys. Lett. **80**, 3922 (2002).

[25] D. Meng, H. Guo, Z. Cui, C. Ma, J. Zhao, J. Lu, H. Xu, Z. Wang, X. Hu, Z. Fu, R. Peng, J. Guo, X. Zhai, G. J. Brown, R. Knize, and Y. Lu, Strain-induced high-temperature perovskite ferromagnetic insulator, Proc. Natl. Acad. Sci. USA **115**, 2873 (2018).

[26] G. Thornton, B. C. Tofield, and A. W. Hewat, A neutron diffraction study of $LaCoO_3$ in the temperature range $4.2<T<1248$ K, J. Solid State Chem. **61**, 301 (1986).

[27] B. H. Frazer, B. Gilbert, B. R. Sonderegger, and G. De Stasio, The probing depth of total electron yield in the sub-keV range: TEY-XAS and X-PEEM, Surf. Sci. **537**, 161 (2003).

[28] B. Liu, C. Piamonteze, M. U. Delgado-Jaime, R.-P. Wang, J. Heidler, J. Dreiser, R. Chopdekar, F. Nolting, and F. M. F. de Groot, Sum rule distortions in fluorescence-yield x-ray magnetic circular dichroism, Phys. Rev. B **96**, 054446 (2017).

[29] F. de Groot, Multiplet effects in x-ray spectroscopy, Coord. Chem. Rev. **249**, 31 (2005).

[30] See Supplemental Material at http://link.aps.org/supplemental/10.1103/PhysRevMaterials.4.026001 for technical details and additional data.

[31] E. Grieten, O. Schalm, P. Tack, S. Bauters, P. Storme, N. Gauquelin, J. Caen, A. Patelli, L. Vincze, and D. Schryvers, Reclaiming the image of daguerreotypes: Characterization of the corroded surface before and after atmospheric plasma treatment, J. Cultural Heritage **28**, 56 (2017).

[32] B. Conings, S. A. Bretschneider, A. Babayigit, N. Gauquelin, I. Cardinaletti, J. Manca, J. Verbeeck, H. J. Snaith, and H.-G. Boyen, Structure-property relations of methylamine vapor treated hybrid perovskite $CH_3NH_3PbI_3$ films and solar cells, ACS Appl. Mater. Interfaces **9**, 8092 (2017).

[33] D. J. Groenendijk, C. Autieri, T. C. van Thiel, W. Brzezicki, N. Gauquelin, P. Barone, K. H. W. van den Bos, S. van Aert, J. Verbeeck, A. Filippetti, S. Picozzi, M. Cuoco, and A. D. Caviglia, Berry phase engineering at oxide interfaces, arXiv:1810.05619.

[34] A. N. Vasiliev, O. S. Volkova, L. S. Lobanovskii, I. O. Troyanchuk, Z. Hu, L. H. Tjeng, D. I. Khomskii, H. J. Lin, C. T. Chen, N. Tristan, F. Kretzschmar, R. Klingeler, and B. Büchner, Valence states and metamagnetic phase transition in partially *B*-site-disordered perovskite $EuMn_{0.5}Co_{0.5}O_3$, Phys. Rev. B **77**, 104442 (2008).

[35] We point out that the very tiny shoulder at the lowest energy in the blue trace of Fig. 2(a) could signal a nonzero divalent contribution, but this is too small to fit reliably. We estimate the divalent contribution to be less than 3%.

[36] The 4/2/4 data are the same as those shown in Fig. 2(a).

[37] J. H. Jang, Y. M. Kim, Q. He, R. Mishra, L. Qiao, M. D. Biegalski, A. R. Lupini *et al.*, *In situ* observation of oxygen vacancy dynamics and ordering in the epitaxial $LaCoO_3$ system, ACS Nano **11**, 6942 (2017).

[38] G. Liu, X. Li, Y. Wang, W. Liang, B. Liu, H. Feng, H. Yang, J. Zhang, and J. Sun, Nanoscale domains of ordered

oxygen-vacancies in $LaCoO_3$ films, Appl. Surf. Sci. **425**, 121 (2017).

[39] V. V. Mehta, N. Biškup, C. Jenkins, E. Arenholz, M. Varela, and Y. Suzuki, Long-range ferromagnetic order in $LaCoO_{3-\delta}$ epitaxial films due to the interplay of epitaxial strain and oxygen vacancy ordering, Phys. Rev. B **91**, 144418 (2015).

[40] J.-H. Kwon, W. S. Choi, Y.-K. Kwon, R. Jung, J.-M. Zuo, H. N. Lee, and M. Kim, Nanoscale spin-state ordering in $LaCoO_3$ epitaxial thin films, Chem. Mater. **26**, 2496 (2014).

[41] W. S. Choi, J.-H. Kwon, H. Jeen, J. E. Hamann-Borrero, A. Radi, S. Macke, R. Sutarto, F. He, G. A. Sawatzky, V. Hinkov, M. Kim, and H. N. Lee, Strain-induced spin states in atomically ordered cobaltites, Nano Lett. **12**, 4966 (2012).

[42] N. Biškup, J. Salafrance, V. Mehta, M. P. Oxley, Y. Suzuki, S. J. Pennycook, S. T. Pantelides, and M. Varela, Insulating Ferromagnetic $LaCoO_{3-\delta}$ Films: A Phase Induced by Ordering of Oxygen Vacancies, Phys. Rev. Lett. **112**, 087202 (2014).

[43] Y. Chen, D. D. Fong, F. W. Herbert, J. Rault, J.-P. Rueff, N. Tsvetkov, and B. Yildiz, Modified oxygen defect chemistry at transition metal oxide heterostructures probed by hard x-ray photoelectron spectroscopy and x-ray diffraction, Chem. Mater. **30**, 3359 (2018).

[44] M. C. Biesinger, B. P. Payne, A. P. Grosvenor, L. W. M. Lau, A. R. Gerson, and R. S. C. Smart, Resolving surface chemical states in XPS analysis of first row transition metals, oxides and hydroxides: Cr, Mn, Fe, Co and Ni, Appl. Surf. Sci. **257**, 2717 (2011).

[45] G. van der Laan, C. Westra, C. Haas, and G. A. Sawatzky, Satellite structure in photoelectron and Auger spectra of copper dihalides, Phys. Rev. B **23**, 4369 (1981).

[46] C. A. F. Vaz, D. Prabhakaran, E. I. Altman, and V. E. Henrich, Experimental study of the interfacial cobalt oxide in Co_3O_4/α-$Al_2O_3(0001)$ epitaxial films, Phys. Rev. B **80**, 155457 (2009).

[47] K. S. Kim, X-ray-photoelectron spectroscopic studies of the electronic structure of CoO, Phys. Rev. B **11**, 2177 (1975).

[48] M. Huijben, G. Koster, M. K. Kruize, S. Wenderich, J. Verbeeck, S. Bals, E. Slooten, B. Shi, H. J. Molegraaf, J. E. Kleibeuker, S. van Aert, J. B. Goedkoop, A. Brinkman, D. H. Blank, M. S. Golden, G. van Tendeloo, H. Hilgenkamp, and G. Rijnders, Defect engineering in oxide heterostructures by enhanced oxygen surface exchange, Adv. Funct. Mater. **23**, 5240 (2013).

[49] B. T. Thole, G. van der Laan, and G. A. Sawatzky, Strong Magnetic Dichroism Predicted in the $M_{4,5}$ X-Ray Absorption Spectra of Magnetic Rare-Earth Materials, Phys. Rev. Lett. **55**, 2086 (1985).

[50] G. Schütz, W. Wagner, W. Wilhelm, P. Kienle, R. Zeller, R. Frahm, and G. Materlik, Absorption of Circularly Polarized X Rays in Iron, Phys. Rev. Lett. **58**, 737 (1987).

[51] B. Thole, P. Carra, F. Sette, and G. van der Laan, X-Ray Circular Dichroism as a Probe of Orbital Magnetization, Phys. Rev. Lett. **68**, 1943 (1992).

[52] S. I. Csiszar, M. W. Haverkort, Z. Hu, A. Tanaka, H. H. Hsieh, H.-J. Lin, C. T. Chen, T. Hibma, and L. H. Tjeng, Controlling Orbital Moment and Spin Orientation in CoO Layers by Strain, Phys. Rev. Lett. **95**, 187205 (2005).

[53] T. Jo and T. Shishidou, Orbital magnetic moments of CoO and FeO and isotropic Co and Fe $L_{2,3}$ absorption spectroscopy, J. Phys. Soc. Jpn. **67**, 2505 (1998).

[54] S. Blundell, *Magnetism in Condensed Matter* (Oxford University Press, Oxford, 2001).

[55] The photon energy dependence of the L XMCD signal for LCO4 shown in Fig. 7(a) is different from that of the samples with interfaces [Figs. 7(b)–7(d)], an additional argument on top of the valence fingerprint data that the spins in LCO4 are not originating from Co(II)-$3d^7$ centers.

[56] C. F. Chang, Z. Hu, H. Wu, T. Burnus, N. Hollmann, M. Benomar, T. Lorenz *et al.*, Spin Blockade, Orbital Occupation, and Charge Ordering in $La_{1.5}Sr_{0.5}CoO_4$, Phys. Rev. Lett. **102**, 116401 (2009).

[57] R. D. Shannon, Revised effective ionic radii and systematic studies of interatomic distances in halides and chalcogenides, Acta Cryst. A **32**, 751 (1976).

[58] Thick LCO films grown on STO ($d_{LCO} = 60$ nm) using similar conditions to those given in Table I did exhibit ferromagnetism, observable using both VSM and element-specific (XMCD) magnetometry, in keeping with the literature for thicker LCO films. The present (ultra)thin cobalt oxide layers may simply be below the minimal thickness required to enable FM ordering, as has been reported for PLD-grown $LaMnO_3$ films in X. R. Wang *et al.*, Imaging and control of ferromagnetism in $LaMnO_3/SrTiO_3$ heterostructures, Science **349**, 716 (2015).

[59] A. Barla, G. Schmerber, E. Beaurepaire, A. Dinia, H. Bieber, S. Colis, F. Scheurer *et al.*, Paramagnetism of the Co sublattice in ferromagnetic $Zn_{1-x}Co_xO$ films, Phys. Rev. B **76**, 125201 (2007).

[60] M. Merz, P. Nagel, C. Pinta, A. Samartsev, H. v. Löhneysen, M. Wissinger, S. Uebe, A. Assmann, D. Fuchs, and S. Schuppler, X-ray absorption and magnetic circular dichroism of $LaCoO_3$, $La_{0.7}Ce_{0.3}CoO_3$, and $La_{0.7}Sr_{0.3}CoO_3$ films: Evidence for cobalt-valence-dependent magnetism, Phys. Rev. B **82**, 174416 (2010).

[61] G. van der Laan, E. Arenholz, R. V. Chopdekar, and Y. Suzuki, Influence of crystal field on anisotropic x-ray magnetic linear dichroism at the Co^{2+}-$L_{2,3}$ edges, Phys. Rev. B **77**, 064407 (2008).

[62] A. Maignan, V. Caignaert, B. Raveau, D. Khomskii, and G. Sawatzky, Thermoelectric Power of $HoBaCo_2O_{5.5}$: Possible Evidence of the Spin Blockade in Cobaltites, Phys. Rev. Lett. **93**, 026401 (2004).